Naval Research Laboratory
Washington, DC 20375-5320

NRL/8220/MR—2022/2

Simulating Unstart in an Axisymmetric, Supersonic Cavity Flameholder

GABRIEL B. GOODWIN

EVAN W. HYDE

CHRISTIAN L. BACHMAN

Hypersonic Aerodynamics and Propulsion Section
Spacecraft Engineering Division

RYAN F. JOHNSON

DAVID A. KESSLER

Laboratories for Computational Physics and Fluid Dynamics Branch
Materials Science and Component Technology Division

April 25, 2022

REPORT DOCUMENTATION PAGE

Form Approved
OMB No. 0704-0188

1. REPORT DATE *(DD-MM-YYYY)* 25-04-2022	**2. REPORT TYPE** NRL Memorandum Report	**3. DATES COVERED** *(From - To)* 10/01/2020 – 09/30/2021

4. TITLE AND SUBTITLE Simulating Unstart in an Axisymmetric, Supersonic Cavity Flameholder	**5a. CONTRACT NUMBER** **5b. GRANT NUMBER** **5c. PROGRAM ELEMENT NUMBER**
6. AUTHOR(S) Gabriel B. Goodwin, Evan W. Hyde, Christian L. Bachman, Ryan F. Johnson, and David A. Kessler	**5d. PROJECT NUMBER** **5e. TASK NUMBER** **5f. WORK UNIT NUMBER** 6C11
7. PERFORMING ORGANIZATION NAME(S) AND ADDRESS(ES) Naval Research Laboratory 4555 Overlook Avenue, SW Washington, DC 20375-5320	**8. PERFORMING ORGANIZATION REPORT NUMBER** NRL/8220/MR--2022/2
9. SPONSORING / MONITORING AGENCY NAME(S) AND ADDRESS(ES) Naval Research Laboratory 4555 Overlook Avenue, SW Washington, DC 20375-5320	**10. SPONSOR / MONITOR'S ACRONYM(S)** NRL 6.2 Base Program **11. SPONSOR / MONITOR'S REPORT NUMBER(S)**

12. DISTRIBUTION / AVAILABILITY STATEMENT

DISTRIBUTION STATEMENT A: Approved for public release; distribution is unlimited.

13. SUPPLEMENTARY NOTES

14. ABSTRACT

Axisymmetric cavity combustors are not subjected to the corner boundary-layer effects present in planar combustors, making them an attractive configuration for robust flameholding. Experiments at the University of Illinois have investigated ethylene combustion in an axisymmetric combustor using a cavity flameholder with inlet flow at Mach 4.5. Cavity flameholding was achieved for a range of fuel equivalence ratios. In the current study, the Naval Research Laboratory's discontinuous Galerkin finite element method code, the JENRE® Multiphysics Framework, was used to simulate combustion in the University of Illinois ACT-II cavity combustor facility. Fuel equivalence ratio was increased from 1.0 until unstart occurred due to thermal choking. The simulations were three-dimensional and an eighth-symmetry domain was used with rotationally periodic boundary conditions in order to reduce computational expense. Simulations were performed both with artificial viscosity and with physical diffusion and the results are compared. The unstart process was initiated at highly fuel-rich conditions due to thermal choking.

15. SUBJECT TERMS

16. SECURITY CLASSIFICATION OF:			**17. LIMITATION OF ABSTRACT**	**18. NUMBER OF PAGES**	**19a. NAME OF RESPONSIBLE PERSON** Gabriel B. Goodwin
a. REPORT U	**b. ABSTRACT** U	**c. THIS PAGE** U	U	19	**19b. TELEPHONE NUMBER** *(include area code)* (202) 404-2710

Standard Form 298 (Rev. 8-98)
Prescribed by ANSI Std. Z39.18

This page intentionally left blank.

CONTENTS

FIGURES

TABLES

EXECUTIVE SUMMARY

Axisymmetric cavity combustors are not subjected to the corner boundary-layer effects present in planar combustors, making them an attractive configuration for robust flameholding. Experiments at the University of Illinois have investigated ethylene combustion in an axisymmetric combustor using a cavity flameholder with inlet flow at Mach 4.5. Cavity flameholding was achieved for a range of fuel equivalence ratios. In the current study, the Naval Research Laboratory's discontinuous Galerkin finite element method code, the JENRE® Multiphysics Framework, was used to simulate combustion in the University of Illinois ACT-II cavity combustor facility. Fuel equivalence ratio was increased from 1.0 until unstart occurred due to thermal choking. The simulations were three-dimensional and an eighth-symmetry domain was used with rotationally periodic boundary conditions in order to reduce computational expense. Simulations were performed both with artificial viscosity and with physical diffusion and the results are compared. The unstart process was initiated at highly fuel-rich conditions due to thermal choking.

This page intentionally left blank

SIMULATING UNSTART IN AN AXISYMMETRIC, SUPERSONIC CAVITY FLAMEHOLDER

1. INTRODUCTION

There has been a resurgence of research in axisymmetric combustors for dual-mode combustion systems due to the enhanced flow uniformity and minimization of corner flow effects as compared to rectangular, planar combustors. Axisymmetric combustors are also attractive for flight vehicles due to their decreased structural weight required to withstand a given pressure and thermal load. Recent computational work investigated the mode transition dynamics in dual-mode combustors in both planar and axisymmetric configurations [1]. It was found that boundary layer separation from corner flow effects dominated the mode transition in the rectangular engine, while the transition from combustion near the primary injectors to the secondary injectors occurred more smoothly in the equivalent axisymmetric configuration. Experiments at the University of Illinois have investigated the combustion dynamics in the ACT-II facility, a Mach 4.5 axisymmetric combustor using ethylene fuel [2–4]. Stable combustion was achieved with both lean and rich global fuel equivalence ratios without unstart. The cavity was found to improve combustor performance through fuel-air mixing rather than by reduction in ignition time through radical recirculation. It was also observed that the cavity promoted the transition of quasi-laminar flame shapes to large-scale turbulent flame structures in the diverging section of the combustor [5].

A series of experiments in ACT-II investigated the potential of the heat release in the combustor to choke the incoming flow [6]. It was determined that combustion produced minimal heat addition in the core flow and the resulting pressure gradient was insufficient to separate the boundary layer; most of the heat addition due to combustion was in the boundary layer, which promoted growth of the boundary layer and confined the core flow. It was determined that this confinement resulted in entropy generation, reducing Mach number in the core region and making choking likely. Dual-mode operation and transition were studied in ACT-II, finding that the initiation of mode transition was dependent on the amount of heat addition relative to the area relief along the axial flowpath of the combustor [7]. Thermal choking was found to begin at the point in the diverging section of the combustor where the effects of combustion heat loading and area relief are relatively comparable. The choking resulted in mode transition and a steady ramjet flow was established with the flow accelerating to supersonic downstream of the cavity ramp. In order for the combustion to remain stable, it was found that the area relief needs to balance the combustion heat loading such that heat release is sufficient to prevent quenching without causing choking [3]. Other work at ACT-II has focused on isolator shock dynamics and unstart [8] as well as laser-induced plasma ignition [9].

Recent work at the Naval Research Laboratory focused on using NRL's discontinuous Galerkin (DG) finite element method code, the JENRE® Multiphysics Framework, to simulate combustion in the ACT-II facility [10]. The simulations in this prior work used an inflow static pressure two orders of magnitude greater than that in the experiments due to the limits of the ethylene-air combustion model selected. In the current study, the chemical model is modified to support combustion at the lower pressure and the simulations reflect actual experimental conditions. Several cases are presented with varying equivalence ratio to show the thermal choking and unstart process at highly fuel-rich conditions. Additionally, results with and without physical diffusion are compared.

Manuscript approved April 8, 2022.

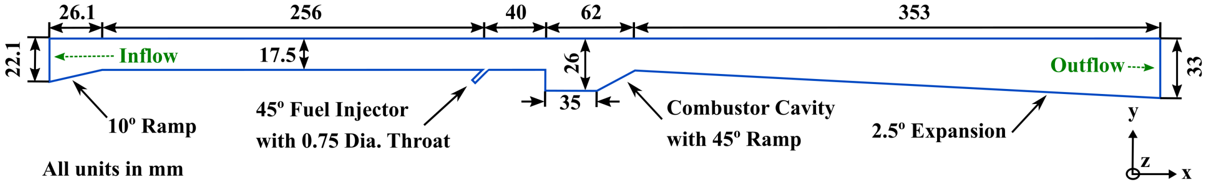

Fig. 1—Schematic of a cross-section of the computational domain.

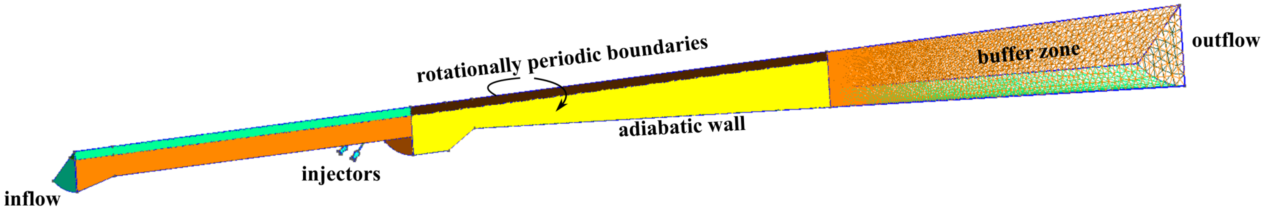

Fig. 2—Computational mesh with boundary conditions.

2. NUMERICAL MODEL

These computations solve the fully conservative formulation of the multi-component, chemically reacting Navier Stokes equations [11], given as,

$$\frac{\partial \rho \boldsymbol{v}}{\partial t} + \nabla \cdot (\rho \boldsymbol{v} \otimes \boldsymbol{v} + p\mathbb{I}) = \nabla \cdot \boldsymbol{\tau}, \tag{1}$$

$$\frac{\partial (\rho e_{\mathrm{t}})}{\partial t} + \nabla \cdot ((\rho e_{\mathrm{t}} + p)\, \boldsymbol{v}) = \nabla \cdot \left(\lambda \nabla T - \sum_{i=1}^{N_{\mathrm{s}}} W_{\mathrm{i}} C_{\mathrm{i}} h_{\mathrm{i}} \mathbf{V}_{\mathrm{i}} + \boldsymbol{\tau} \cdot \boldsymbol{v} \right), \tag{2}$$

$$\frac{\partial C_{\mathrm{i}}}{\partial t} + \nabla \cdot (C_{\mathrm{i}} (\boldsymbol{v} + \mathbf{V}_{\mathrm{i}})) = \omega_{\mathrm{i}} \text{ for } i = 1 \ldots N_{\mathrm{s}}, \tag{3}$$

where ρ is density, $\boldsymbol{v}$ is velocity, p is pressure, $\mathbb{I}$ is an identity matrix, $\boldsymbol{\tau}$ is the deviatoric stress tensor as defined in Eq. (2.17) in [11], e_{t} is total energy, λ is conductivity, T is temperature, N_{s} is the number of species, W_{i} is molecular weight, C_{i} is concentration, h_{i} is enthalpy, $\mathbf{V}_{\mathrm{i}}$ is diffusion velocity, ω_{i} is the production source term, and subscript i indicates species i. The production source term is calculated from the progress reaction rates for any number of reactions and reaction types. Pressure is given by the equation of state,

$$p = R^{o} T \sum_{i=1}^{N_{\mathrm{s}}} C_{\mathrm{i}}, \tag{4}$$

where R^o is the universal gas constant. The species diffusion velocity is given by

$$\mathbf{V}_{\mathrm{i}} = \frac{D_{\mathrm{i}}}{C_{\mathrm{i}}}\nabla C_{\mathrm{i}} - \frac{D_{\mathrm{i}}}{\rho}\nabla \rho, \tag{5}$$

where D_{i} is the mass-averaged diffusion coefficient. All transport coefficients are calculated using mixture-averaged approaches [12–14]. As demonstrated in [11], no artificial viscosity, stabilization, or filtering methods were required to stabilize the multi-component, chemically reacting flows simulated in this work.

In this model, the total energy is defined as

$$\rho e_{\mathrm{t}} = \rho u + \frac{1}{2}\rho \boldsymbol{v} \cdot \boldsymbol{v}, \tag{6}$$

where u is total energy. Internal energy can be defined as a function of total enthalpy, $\rho u = \rho h_{\mathrm{t}} - p$, where h_{t} is total enthalpy and $\rho h_{\mathrm{t}} = \sum_{i=1}^{N_{\mathrm{s}}} W_{\mathrm{i}} C_{\mathrm{i}} h_{\mathrm{i}}$, where h_i is a nonlinear function with respect to temperature.

Equations (1–3) are discretized using the DG method. The resulting DG space semi-discretization, Eq. (3.6) of [11], is integrated temporally with a second order strong-stability-preserving Runge-Kutta method [15]. The temporal integration of the source term is separated from the temporal integration of the conservation laws via Strang operator splitting. The resulting system of ordinary differential equations, describing the influence of the source term on the temporal evolution of the state, is integrated using a temporal and polynomial basis adaptive DG method, DGODE [11]. A seven-species, three-reaction-step reduced chemical mechanism (the global flamespeed mechanism presented in [16]) is used to model the ethylene-air combustion.

3. PROBLEM SET-UP

Figure 1 shows a cross section of the computational domain, sliced through an x-y plane that intersects an injector. The meshed 3D (three-dimensional) domain is shown in Fig. 2. The 3D domain is a $1/8^{\mathrm{th}}$ symmetry slice of the ACT-II axisymmetric combustor facility, including two of the facility's 16 circumferentially positioned fuel injectors. The spanwise boundaries are rotationally periodic. The inflow conditions reproduce those in the ACT-II experiments discussed in [2]; the supersonic inflow boundary is air at 436 K and 500 Pa at a speed of Mach 4.5. In the experiments, trace amounts of NO and O were measured downstream of the arcjet heater. Due to the simplicity of the global ethylene-air combustion mechanism used in these simulations, these trace species were neglected in the inflow gas composition. Consideration of the effects of these species on the combustion process is the subject of future work.

The fuel injectors are stagnation inlets with an inflow of ethylene at 300 K, where stagnation pressure is set to provide the desired equivalence ratio. For the stoichiometric case, this requires a stagnation pressure of 59.5 kPa. The stagnation pressure was increased in order to simulate higher equivalence ratios. The isolator, combustor, and nozzle walls are modeled using slip surfaces in the simulations using artificial viscosity. They were modeled using no-slip, adiabatic surfaces in the simulation computing physical diffusion, as discussed later in this section. The buffer zone, labeled in Fig. 2, is a diffuse region between the combustor and a supersonic outflow boundary. The boundaries of the buffer zone are slip walls, which allow the subsonic flow in the boundary layers in the combustor to accelerate to a supersonic velocity prior to making contact with the supersonic outflow boundary. This was done to improve computational stability at the outflow boundary.

Three different levels of spatial resolution were used for the various simulation cases performed in this study. Table 1 shows the equivalence ratio, DG tetrahedral element order of accuracy, and regional element size for all of the cases. All cases were performed using the same resolution, with the exception of two of the simulations with an equivalence ratio of 1.0; here, the solution was run to steady state on the base grid (case 1), then the grid was refined by doubling the number of elements uniformly across the domain (case 2), then the order of accuracy of elements was increased from second to third order (case 3). The base resolution was used for the remainder of the cases. The coarse (case 1) and fine (case 3) solutions are compared in the following section and the coarse mesh is shown to adequately resolve all features of interest.

The element sizes in the various regions of the mesh were selected to balance spatial resolution with computational expense. All of the simulations, with the exception of case 3, were inviscid with with some artificial viscosity applied across shocks in order to maintain stability. Case 3 was performed with both an inviscid solution as well as a solution to the viscous Navier-Stokes equations in which physical diffusion was computed, as outlined in Sec. 2. Each case was run until the solution reached a steady state. In case 8, unstart occurs and a normal shock propagates upstream in the isolator. The simulation was stopped shortly before the shock impacted the inflow boundary.

Table 1—Equivalence ratio, element order-of-accuracy, and regional element size for each simulation case.

Case No.	1	2	3	4	5	6	7	8
Equivalence Ratio	1.0	1.0	1.0	1.25	1.5	2	10	20
DG Element Polynomial Order (p)	1	1	2	1	1	1	1	1
Injector Element Size (μm)	240	120	120	240	240	240	240	240
Cavity Element Size (μm)	400	200	200	400	400	400	400	400
Boundary Layer Element Size (μm)	533	266	266	533	533	533	533	533
Freestream Element Size (μm)	800	400	400	800	800	800	800	800

4. RESULTS & DISCUSSION

Case 3, shown in Fig. 3, is inviscid with some artificial viscosity applied across shocks in order to maintain stability. The equivalence ratio is 1.0. The contours were sampled at an x-y plane that intersects one of the fuel injectors. Two views are presented: the entire domain and a focused look at the injector and cavity region. An oblique shock train forms, beginning as the Mach 4.5 inflow is deflected by the inlet ramp. This shock train propagates down the length of this isolator and is most visible in the Mach contours. As this case is inviscid, no boundary layer forms along the walls. The air flowing through the isolator collides with the injected fuel and a shock forms around the fuel jet. This interaction is most readily observed in the cavity close-up portion of Fig. 3.

Contours of Y_{C2H4} show the fuel as it flows from the injector into the isolator and downstream into the cavity shear layer. The fuel does not ignite until it reaches the cavity leading edge, where the fuel passes through a shock that is anchored to the leading edge. The increase in pressure and temperature across this shock is sufficient to ignite the fuel, resulting in the formation of a flame that remains anchored to the cavity leading edge. There is a sharp gradient in temperature from a high temperature region within the cavity to lesser temperature above the cavity shear layer, followed by a second gradient from low to high temperature above the cavity shear layer. It is in these two locations of steepest temperature gradient where combustion occurs. There is a mixture of high temperature fuel and product in the cavity, as is visible in the Y_{C2H4} and Y_{CO2} contours. The flame that sits above the cavity shear layer is also the location of the highest concentration of Y_{CO2}. This flame propagates downstream and remains near the bottom wall.

Figure 4 shows 3D isosurfaces of some quantities of interest for case 3. All isosurfaces are colored by the z component of the surface's unit normal vector. It is apparent that the fuel-air mixture ignites as it passes through the shock anchored to the cavity leading edge, visible in the Mach 3 isosurface. The 3000 K temperature isosurface shows the recirculation of hot combustion products in the cavity, assisting with flame stabilization above the cavity shear layer. The path of the ethylene fuel from injection into the isolator to the cavity, where the ethylene begins to react, is visible in the ethylene isosurfaces. The 2300 K temperature isosurface shows the flame location, where it remains anchored above the cavity shear layer. The fuel jets are incident with this isosurface. Another view of the flame is provided in the Y_{H2O} isosurface; the fuel jets are incident with this as well. The Y_{H2O} surface initially has the tubular shape of the fuel jets, before it flattens downstream of the cavity where the flame develops curvature and wrinkling begins to occur. Finally, the figure shows isosurfaces of Q-criterion. The Q-criterion is commonly used to identify and visualize vortices, defined as connected fluid with a positive second invariant of $\nabla \boldsymbol{v}$ and where the vorticity magnitude is greater than the strain rate magnitude,

$$Q \equiv \frac{1}{2}(v_{i,i}^2 - v_{i,j}v_{j,i}) > 0, \tag{7}$$

where the comma in the subscript denotes differentiation [17]. Figure 4 shows isosurfaces of $Q = 1$, selected to visualize an abundance of vortices of varying length scales throughout the domain. Figure 5 provides a close-up view of the composite image of the isosurfaces labeled in Fig. 4.

Figure 6 shows the Mach and temperature contours for the steady state solution in the injector and cavity regions for cases 1 and 3, corresponding to the inviscid equivalence ratio = 1 simulations with coarse and fine spatial resolution. All of the features of interest, including shocks, shear layers, and flames have nearly identical locations between the two cases. The gradients across these features are also of comparable magnitude between the two cases. These features are clearly more well-resolved in case 3, particularly the shocks and cavity shear layer, but they are all captured nonetheless in the coarser case. The coarser resolution was deemed adequate for the majority of the cases performed, as the goal of this study was to observe the flame stability and movement of the flame within the combustor as a function of equivalence ratio. A secondary goal was to capture the unstart phenomenon, if it could be generated through increasing the equivalence ratio to the point of thermal choking.

Case 3 was also performed with physical diffusion. The inviscid case 3 solution, described in the above paragraphs, was used as the initial condition for the simulation with physical diffusion, which was then run to a steady state. Figure 7 shows contours of case 3 computed with physical diffusion. In this simulation, all wall boundaries are no-slip surfaces and the remaining boundaries were the same as previously described.

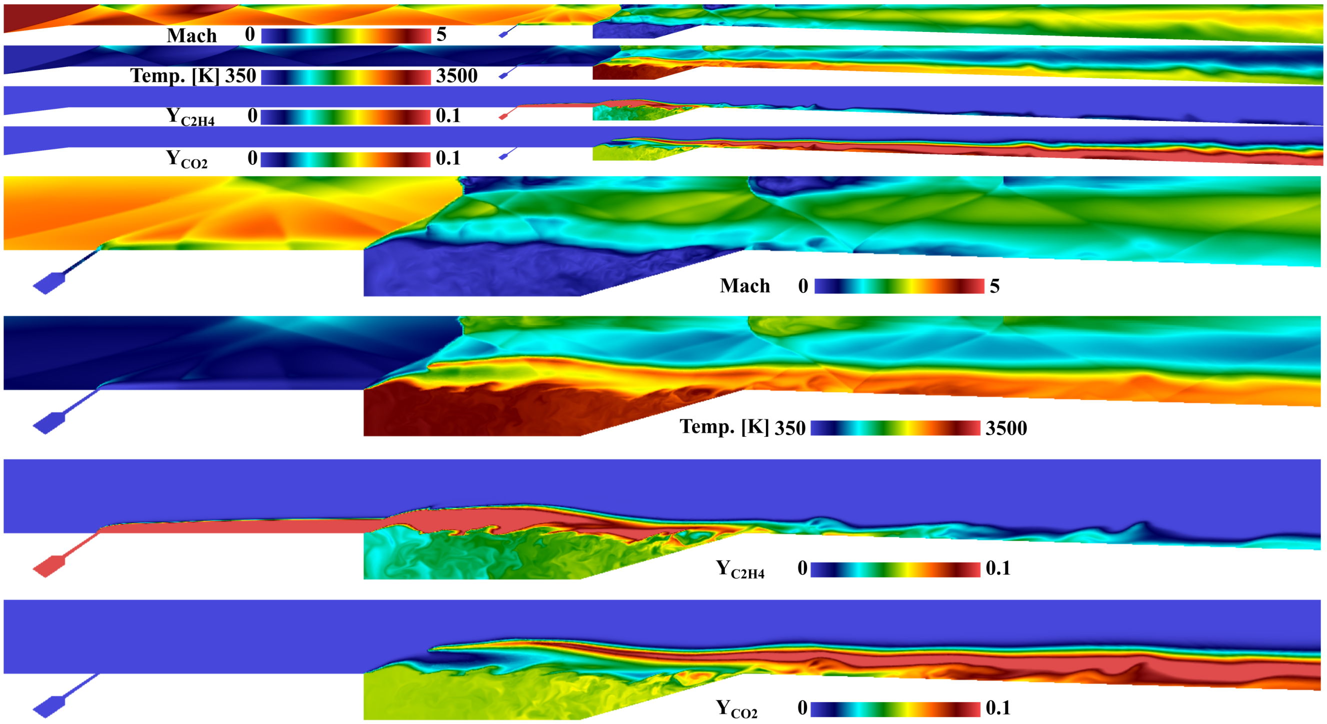

Fig. 3—Contours of Mach number, temperature, ethylene mass fraction, and carbon dioxide mass fraction for case 3 with artificial viscosity. Lower images show close-up of injector/cavity region.

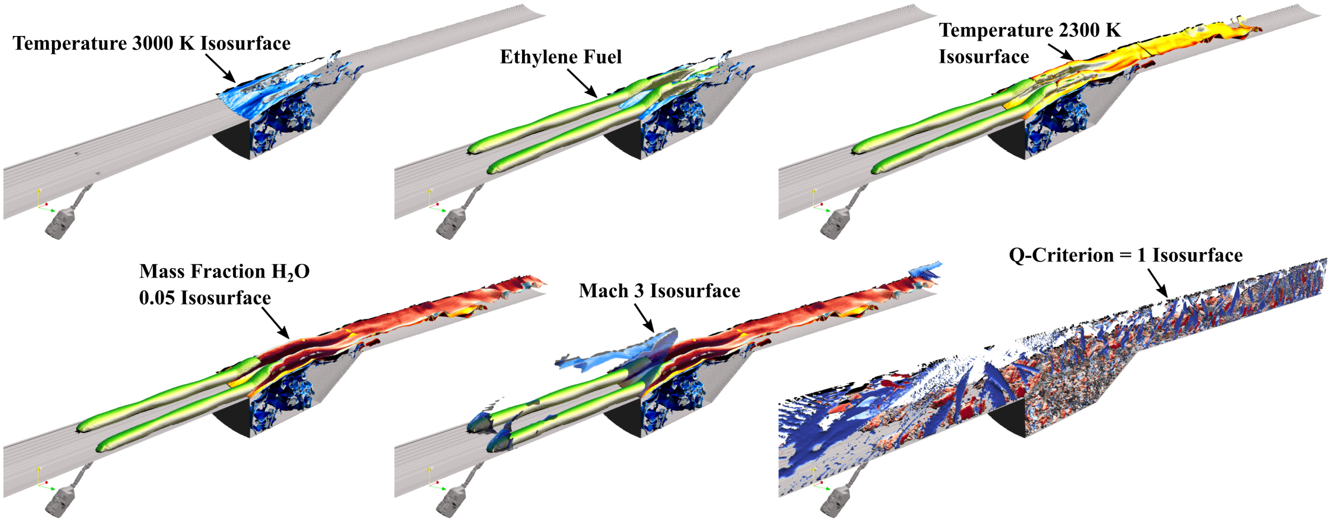

Fig. 4—3D isosurfaces show flame structure in the case 3 simulation with artificial viscosity. Same time step as shown in Fig. 3.

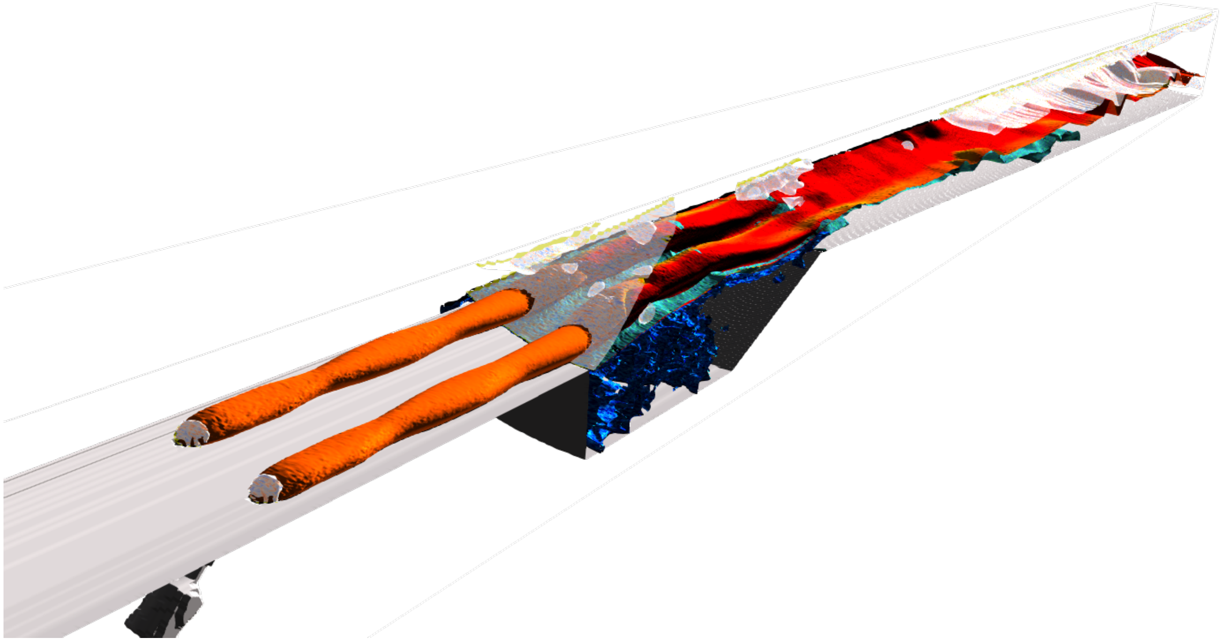

Fig. 5—Composite image of 3D isosurfaces for the case 3 simulation with artificial viscosity.

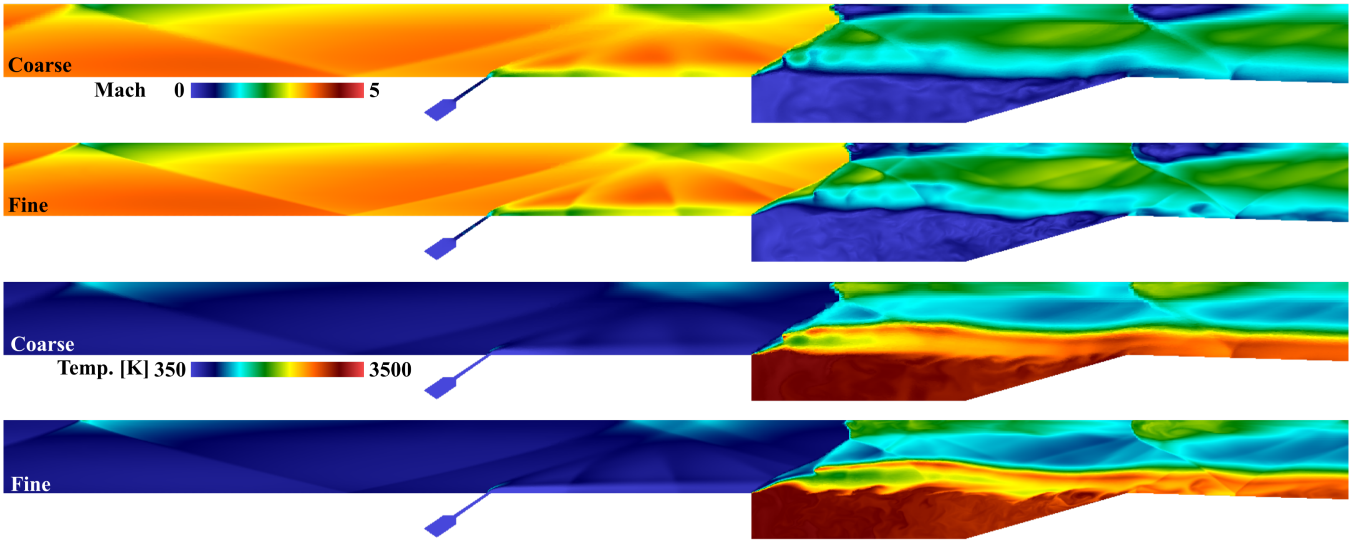

Fig. 6—Comparison of solutions with fine (case 3) and coarse (case 1) resolution for an equivalence ratio of 1.

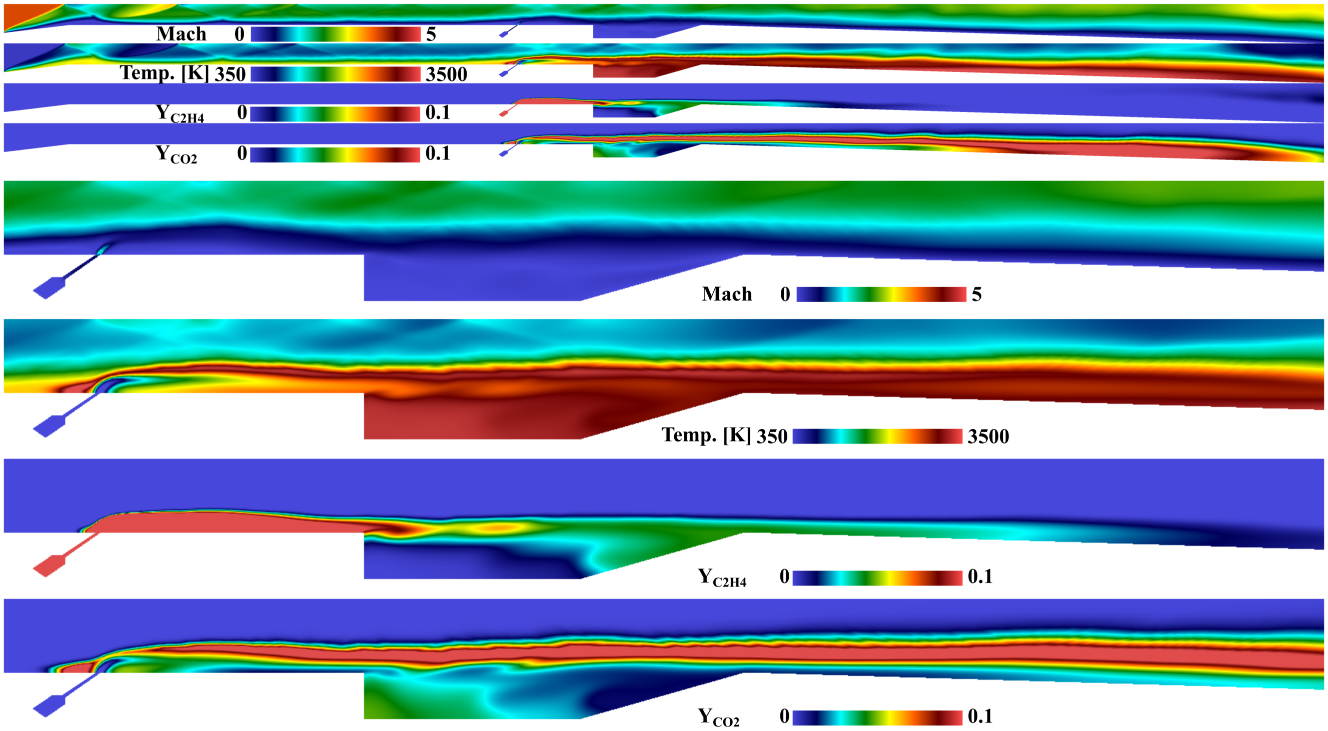

Fig. 7—Contours of Mach number, temperature, ethylene mass fraction, and carbon dioxide mass fraction for the case 3 solution with physical diffusion. Lower images show close-up of injector/cavity region.

Here, the fuel ignites at the fuel-air interface immediately upstream of the fuel jet where it enters the isolator. This reaction begins when the high temperature air in the boundary layer impacts the fuel jet. The flame remains stable in the cavity shear layer and downstream for the duration of the simulation. The flame itself is also more diffuse, as indicated by the Y_{CO2} contours. Although the ignition location differs between the two cases, the flame remains stabilized in the cavity shear layer in both.

One of the notable differences between the inviscid and viscous calculations is the sharpness of the fluid structures, especially the shocks in the fuel jet region and vortices within the cavity. In the viscous simulation, the shocks are much more diffuse and there are no defined structures visible in the cavity. This result is not unexpected, as the species diffusion coefficients scale inversely to pressure and the inflow pressure for this configuration is extremely low at 500 Pa. Figure 8 shows 3D isosurfaces of notable quantities for the viscous case. The ignition of the fuel-air mixture at the fuel-air interface upstream of the fuel jet is evident here. The flame does not appear as wrinkled as it does in the inviscid case, again due to the increased diffusion at the lower pressure conditions. The remaining simulations in this work were performed without physical diffusion.

One of the goals in undertaking this series of computations was to simulate unstart caused by thermal choking in the combustor. Additional computations were performed with equivalence ratios of 1.25, 1.5, 2, 10, and 20, corresponding to cases 4 – 8 in Table 1. Equivalence ratio was modulated by control of the mass flowrate of the injector inflow conditions. The solutions in cases 4 and 5 were nearly identical to case 3 and are not discussed here in detail. Figure 9 shows the steady state solution in case 6 with an equivalence ratio

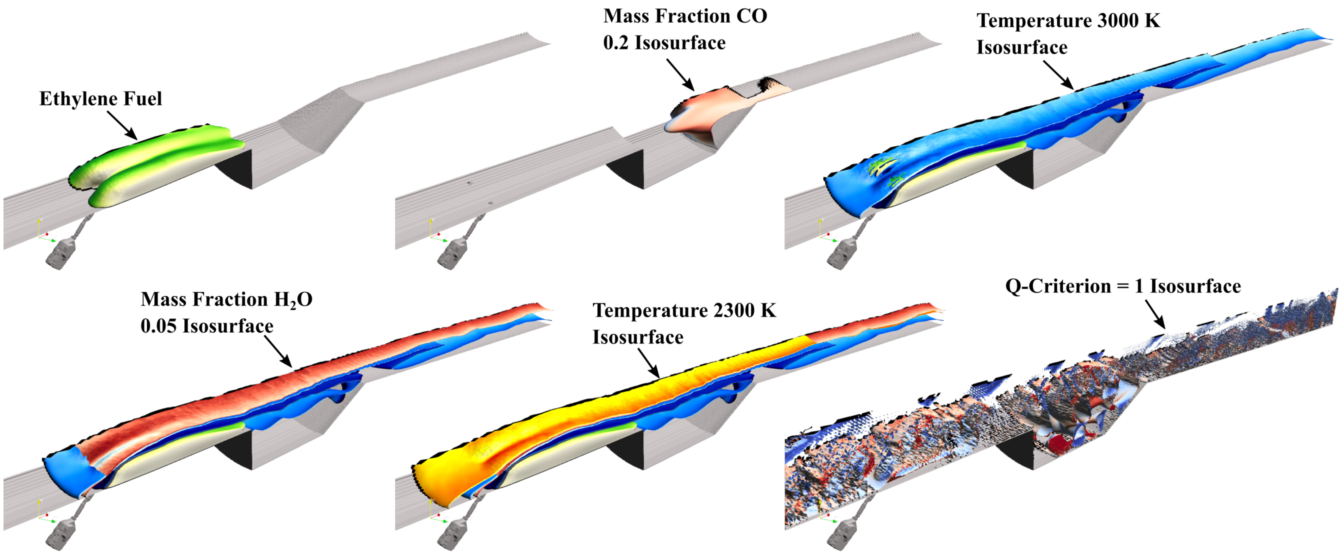

Fig. 8—3D isosurfaces show flame structure in the case 3 simulation with physical diffusion. Same time step as shown in Fig. 7.

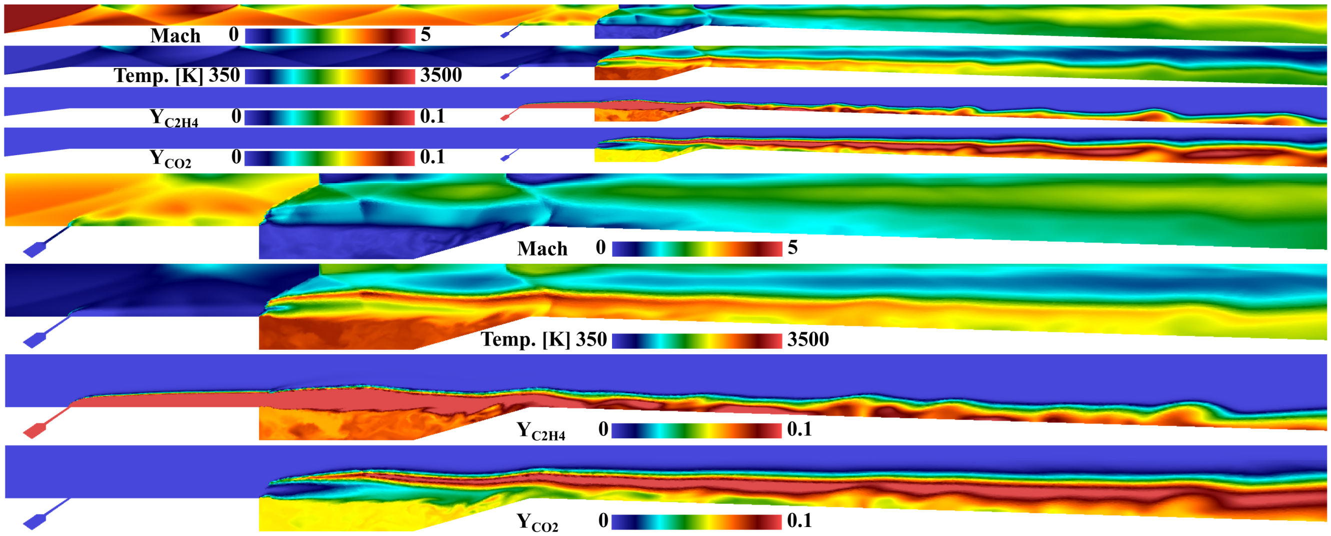

Fig. 9—Contours of Mach number, temperature, ethylene mass fraction, and carbon dioxide mass fraction for case 6.

of 2. The contours show a similar flow to that in case 3 with an equivalence ratio of 1, shown in Fig. 3. The shocks in the vicinity of the fuel injection are in the same locations, though they appear to be slightly more diffuse in case 6 due to the decreased spatial resolution compared to that in case 3. The local Mach in the cavity is subsonic, with supersonic flow above the cavity shear layer. The temperature of the gas entrained in the cavity is lower in case 6 than in case 3, which is the result of the higher mass flowrate of 300 K fuel. The Y_{C2H4} contours show a greater entrainment of fuel in the cavity in the higher equivalence ratio case, which is an expected result of the increased fuel flowrate. The fuel jet also penetrates slightly higher into the core flow here as well. The flame is anchored closer to the leading edge of the cavity, as indicated by the Y_{CO2} contours, where the ribbon of burned product initiates at the cavity leading edge, as opposed to downstream as in case 3. Despite these differences in the combustion between the two cases, the increase in equivalence ratio from 1 to 2 was insufficient to induce thermal choking and unstart.

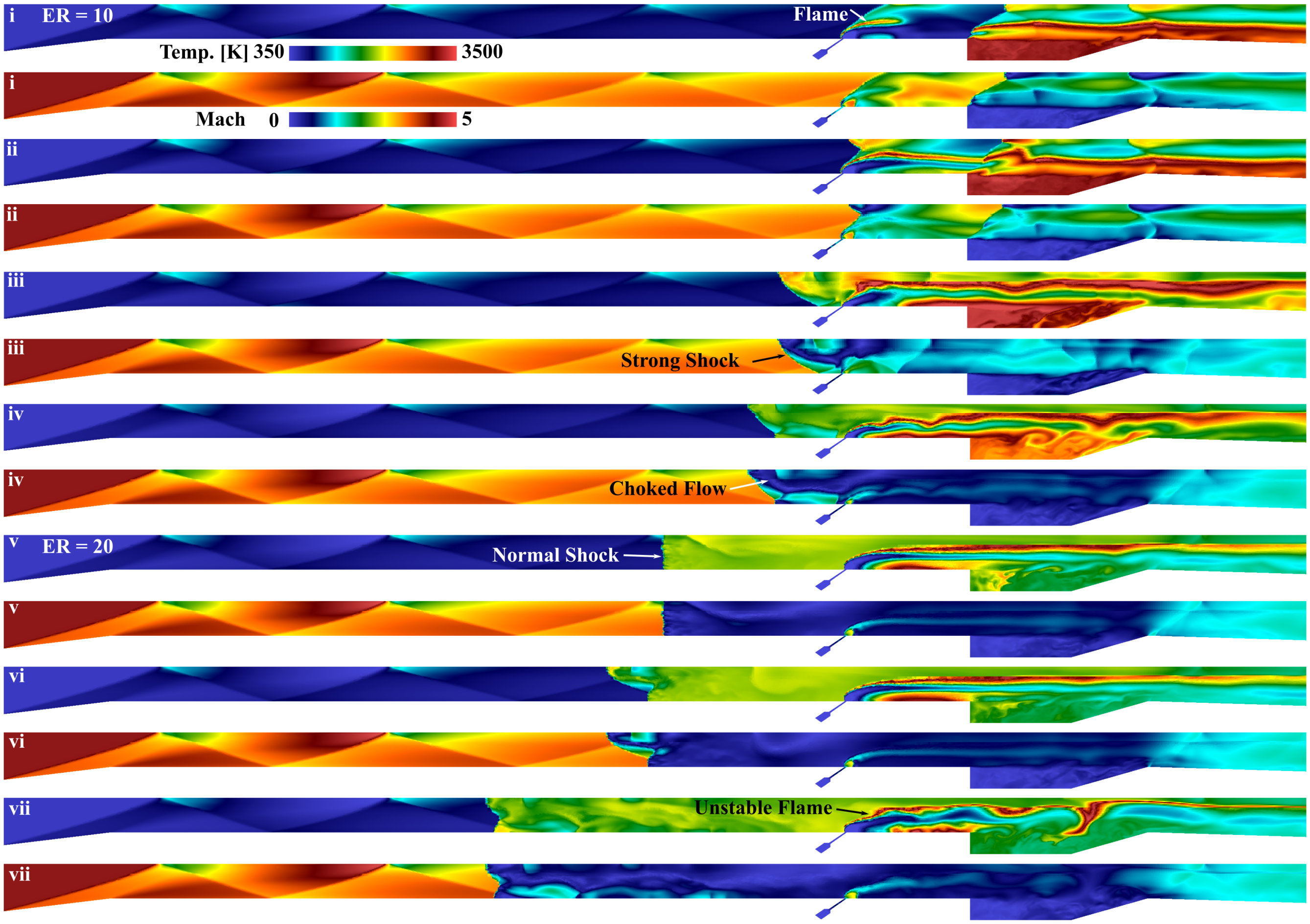

Fig. 10—Temperature and Mach contours for several time steps in cases 7 and 8 illustrate the thermal choking and unstart process.

The equivalence ratio was increased to 10 in the next case performed, case 7. Full unstart was still not observed at this equivalence ratio, so it was increased further to 20 in the final case performed, case 8. Figure 10 shows temperature and Mach contours for seven time steps; steps i – iv are from case 7 and steps v – vii are from case 8. Step i was sampled shortly after the fuel mass flowrate was increased in order to achieve a global equivalence ratio of 10. In step i, a strong shock forms as the isolator crossflow

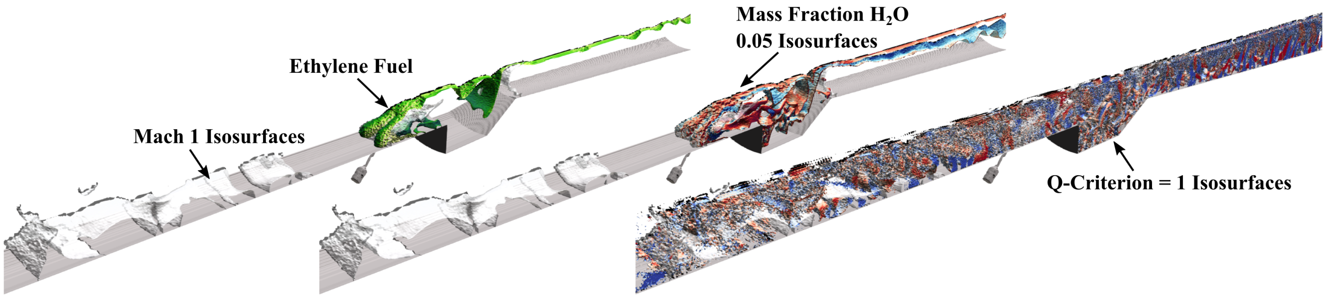

Fig. 11—3D isosurfaces show the presence of several strong shocks upstream of the fuel jet in case 8.

impacts the fuel jet. The temperature increase across the shock is sufficient to cause the fuel jet to autoignite immediately upon penetration into the isolator crossflow. The flame remains relatively stable as the fuel jet shock propagates upstream, as seen in steps ii and iii. When the shock reaches the position shown in step iv, the flow stabilizes and the shock remains stationary. Although the flow through the combustor is choked at this time, as indicated by the subsonic flow behind the shock (labeled in step iv), because the flame remains stable this was not considered a full unstart scenario.

In case 8, where the global equivalence ratio was increased to 20, the increased fuel mass flow into the isolator results in greater backpressure, forcing the strong shock in step iv to move upstream and transition to a normal shock. The normal shock continues to propagate upstream before settling temporarily at the location shown in step v. Here, the normal shock moves upstream very slowly. When it intersects the oblique shock reflecting against the top boundary, visible in step v, it is accelerated further upstream as shown in steps vi and vii. The shock continues upstream until impact with the inflow boundary. The flow between the normal shock and the end of the cavity ramp is entirely subsonic and the flame becomes unstable as the shock continues to propagate upstream. Here, it is evident that unstart is occurring.

Figure 11 shows 3D isosurfaces of interest for time step vii in case 8. The Mach 1 isosurfaces illustrate the presence of several strong shocks in the isolator, which shock the flow in the injector and cavity region to subsonic. The fuel jet is shown, as well as Y_{H2O} isosurfaces which approximate the flame location. It is worth noting that combustion is occuring both above and below the fuel jet, indicating that air flows around the fuel jets and becomes entrained in the cavity. The Q-criterion isosurfaces are more densely populated in this case than in the previously shown cases, likely due to a greater abundance of vortices.

5. CONCLUSIONS

Three-dimensional discontinuous Galerkin CFD simulations of combustion in the University of Illinois ACT-II cavity combustor facility were performed with ethylene fuel at equivalence ratios ranging from 1 to 20. The computational domain was a 1/8 symmetry slice of the experimental facility, including the modeling of two circumferential fuel injectors just upstream of the cavity flameholder. The Mach 4.5 inflow conditions were selected in order to reproduce experimental conditions in the facility. A three-step, seven-species global ethylene-air combustion model was used and simulations were performed both with and without physical diffusion. In the cases without physical diffusion, artificial viscosity was applied across shocks and the walls were slip boundaries. In the case with physical diffusion, the walls were no-slip, adiabatic boundaries.

Global fuel equivalence ratio was modulated by changing the stagnation pressure of the ethylene at the injector inflow boundary, which was a stagnation inlet.

In the cases without physical diffusion and equivalence ratios of 1 to 2, the fuel ignited as it passed through a shock anchored to the leading edge of the cavity combustor. A single case was performed with physical diffusion and an equivalence ratio of 1 was used. Here, the fuel ignited immediately upon entering the isolator crossflow due to the collision of the high-temperature boundary layer with the fuel jet. In this case, the flame remained anchored to the fuel jet. Both with and without physical diffusion, the flame was stabilized by the cavity, where high-temperature fuel and product circulated, promoting combustion in the cavity shear layer. The flame anchoring provided by the cavity design was robust across a wide range of equivalence ratios explored in this study, from 1 to 10, though at 10 the flow became thermally choked. Despite thermally choking when the equivalence ratio was increased from 2 to 10, as indicated by the presence of a strong shock in the isolator with subsonic flow behind, the flame remained stable and anchored to the fuel jet. When the equivalence ratio was further increased from 10 to 20, the shock in the isolator strengthened to a normal shock and propagated upstream. At this point, the flame was no longer stable and the combustor was fully unstarted.

All of the fluid structures, including the shocks, vortices, shear layers, and the flame, were significantly more diffuse in the case with physical diffusion compared to the case without. This is due to the species diffusion coefficients being inversely proportional to pressure and the pressure in the ACT-II facility in the configuration studied is near-vacuum at 500 Pa. This presented a challenging obstacle for simulating this configuration using physical diffusion. Future work will consider this configuration and similar combustors at flight-realistic pressure and temperature conditions such that the simulations can be more readily performed with physical diffusion and a more accurate solution may be obtained. Additionally, diffusion models designed for low-pressure conditions will also be considered.

ACKNOWLEDGMENTS

This work was made possible through the Base Program at the U.S. Naval Research Laboratory.

REFERENCES

1. R. J. Yentsch and D. V. Gaitonde, “Comparison of Mode-Transition Phenomena in Axisymmetric and Rectangular Scramjet Flowpaths,” Proceedings of the 52nd Aerospace Sciences Meeting, 2014, p. 0625.

2. Q. Liu, D. Baccarella, W. Landsberg, A. Veeraragavan, and T. Lee, “Cavity flameholding in an optical axisymmetric scramjet in Mach 4.5 flows,” *Proceedings of the Combustion Institute* **37**(3), 3733–3740 (2019).

3. Q. Liu, D. Baccarella, B. McGann, and T. Lee, “Cavity-enhanced combustion stability in an axisymmetric scramjet model,” *AIAA journal* **57**(9), 3898–3909 (2019).

4. Q. Liu, D. Baccarella, and T. Lee, “Combustion Stabilization in an Axisymmetric Scramjet in Mach 4.5 Flows,” Proceedings of the AIAA Scitech 2019 Forum, 2019, p. 1681.

5. Q. Liu, D. Baccarella, G. Lee, and T. Lee, “Influences of Cavity on Combustion Stabilization in an Axisymmetric Scramjet,” Proceedings of the AIAA Scitech 2019 Forum, 2019, p. 1681.

6. D. Baccarella, Q. Liu, B. J. McGann, and T. Lee, "Combustion Induced Choking and Unstart Initiation in a Circular Constant-Area Supersonic Flow," *AIAA journal* **57**(12), 5365–5376 (2019).

7. Q. Liu, D. Baccarella, B. McGann, and T. Lee, "Dual-Mode Operation and Transition in Axisymmetric Scramjets," *AIAA Journal* **57**(11), 4764–4777 (2019).

8. D. Baccarella, Q. Liu, B. McGann, and T. Lee, "Isolator Shock Dynamics of Mass Injection-Induced Unstart in a Circular Model Scramjet," Proceedings of the 23rd AIAA International Space Planes and Hypersonic Systems and Technologies Conference, 2020.

9. D. Baccarella, G. S. Lee, Q. Liu, G. S. Elliott, J. B. Freund, and T. Lee, "Laser-induced plasma ignition experiments in a direct-connect supersonic combustor at Mach 3," *Journal of Propulsion and Power* pp. 1–12 (2020).

10. E. W. Hyde, G. B. Goodwin, R. F. Johnson, and T. Lee, "Ethylene Combustion in an Axisymmetric Mach 4.5 Cavity," Proceedings of the AIAA Scitech 2021 Forum, 2021, p. 1467.

11. R. F. Johnson and A. D. Kercher, "A Conservative Discontinuous Galerkin Discretization for Chemically Reacting Navier Stokes Equations," *J. Comput. Phys.* **423** (2020).

12. C. R. Wilke, "A Viscosity Equation for Gas Mixtures," *J. Chem. Phys* **18**, 517–519 (04 1950).

13. S. Mathur, P. K. Tondon, and S. C. Saxena, "Thermal conductivity of binary, ternary and quaternary mixtures of rare gases," *Molecular Physics* **12**, 569–579 (1967).

14. R. J. Kee, J. A. Miller, G. H. Evans, and G. Dixon-Lewis, "A computational model of the structure and extinction of strained, opposed flow, premixed methane-air flames," *Proc. Combust. Inst.* **22**(1), 1479–1494 (1989).

15. S. Gottlieb, C. Shu, and E. Tadmor, "Strong stability-preserving high-order time discretization methods," *SIAM review* **43**(1), 89–112 (2001).

16. D. M. Peterson, "High-Resolution Simulations of Premixed Combustion in a Supersonic Cavity," Proceedings of the AIAA Scitech 2019 Forum, 2019, p. 0448.

17. V. Kolář, "Vortex identification: New requirements and limitations," *International Journal of Heat and Fluid Flow* **28**, 638–652 (2007).